LRP 405/90 MAY 1990

AXISYMMETRIC MHD EQUILIBRIUM SOLVER WITH BICUBIC HERMITE ELEMENTS

H. Lütjens, A. Bondeson and A. Roy

submitted for publication in
Computer Physics Communications

Axisymmetric MHD Equilibrium Solver with Bicubic Hermite Elements

H. Lütjens, A. Bondeson, A. Roy

Centre de Recherches en Physique des Plasmas
Association Euratom - Confédération Suisse
Ecole Polytechnique Fédérale de Lausanne
21, av. des Bains – CH-1007 Lausanne/Switzerland

May 4, 1990

Abstract

A numerical code solving axisymmetric magnetohydrodynamic equilibria with rectangular bicubic Hermite elements has been developed. Two test cases are used for checking the convergence rate of the solution. The mapping of the equilibrium quantities into flux coordinates for magnetohydrodynamic stability calculation is performed by a method which preserves the convergence properties of the cubic Hermite elements. Convergence studies show the behaviour of the stability results when the equilibrium mesh is varied.

1 Introduction

The study of ideal and resistive linear magnetohydrodynamic (MHD) instabilities in toroidal configurations requires accurate solutions of the equilibrium equations. Most existing equilibrium codes use finite linear hybrid elements [1] or finite differences [2], where the solution converges like the square of the mesh size. However, in many cases of interest, the number of intervals required is such that the calculation becomes too expensive in computer time. One possible way to avoid this problem is to use Fourier decomposition in the poloidal plane [3], where the error decreases exponentially with the poloidal mode number. Another solution is a higher order finite element approach. In this work, we present a new numerical code, called CHEASE ((C)ubic (H)ermite (E)lement (A)xisymmetric (S)tatic MHD (E)quilibrium solver), which solves the Grad-Schlüter-Shafranov equation for a fixed boundary plasma, using bicubic Hermite finite elements on rectangles, and provides equilibria for the two stability codes ERATO [4] and MARS [5].

With bicubic Hermite elements, the error on the solution converges as

$$\|\Psi - \Psi_h\| < Ch^4 \tag{1}$$

where C is a constant, and the energy of the poloidal magnetic field converges proportional to $\mathcal{O}(h^6)$ [7]. The Grad-Schlüter-Shafranov equation is an ideal candidate for higher order elements, because its solution is generally very smooth.

The Hermite bicubic elements ensure that the gradient of the solution is continuous over the whole equilibrium mesh, which makes easier a precise localisation of the magnetic axis $|\nabla\Psi| = 0$, even for an asymmetric plasma cross-section. Furthermore, they guarantee that the second derivative of the solution converges within every cell of the mesh, which is very important for the stability calculations.

In section 2, we give basic definitions and outline the method of solution. In the following two sections, we show convergence tests with CHEASE. These fall into two different categories:

1. Computation of the solution of the Grad-Schlüter-Shafranov equation (Section 3). Convergence studies for the poloidal magnetic energy are presented for a Solovev equilibrium [8], and for a nonlinear equilibrium with JET (Joint European Torus) plasma cross-section. In addition, for the Solovev case, we study the convergence of the magnetic flux towards its analytic solution.

2. Mapping of the equilibrium to flux coordinates for stability calculations (Section 4). The two test cases used to check the Grad-Schlüter-Shafranov equation are unstable equilibria. The accuracy of the mapping has been verified in both cases by studying how the growth rates of the instabilities computed by ERATO and MARS converge when the equilibrium mesh is varied.

2 Physical Problem

2.1 Basic Equations

In a static ideal equilibrium, the MHD equations reduce to

$$\begin{aligned} \nabla p &= (\nabla \times \boldsymbol{B}) \times \boldsymbol{B} \\ \nabla \cdot \boldsymbol{B} &= 0 \end{aligned} \tag{2}$$

where p and $\boldsymbol{B}$ denote respectively the plasma pressure and the magnetic field. For a study of tokamak equilibria, we use cylindrical coordinates (r, z, ϕ) (see figure 1) and only consider axisymmetric solutions with $\partial/\partial\phi = 0$. The general solution for the magnetic field which fullfils equation (2) in axisymmetric geometry [6] can be written in terms of the poloidal magnetic flux Ψ and the toroidal magnetic flux T :

$$\boldsymbol{B} = T\nabla\phi + \nabla\phi \times \nabla\Psi \tag{3}$$

Introducing (3) into (2) leads to the Grad-Schlüter-Shafranov equation

$$\nabla\left\{\frac{\nabla\Psi}{r^2}\right\} = \frac{j_\phi}{r} = -\frac{dp}{d\Psi} - \frac{1}{2r^2}\frac{dT^2}{d\Psi} \tag{4}$$

where T^2 and p are functions of $\Psi(r, z)$ only, and j_ϕ represents the toroidal current density.

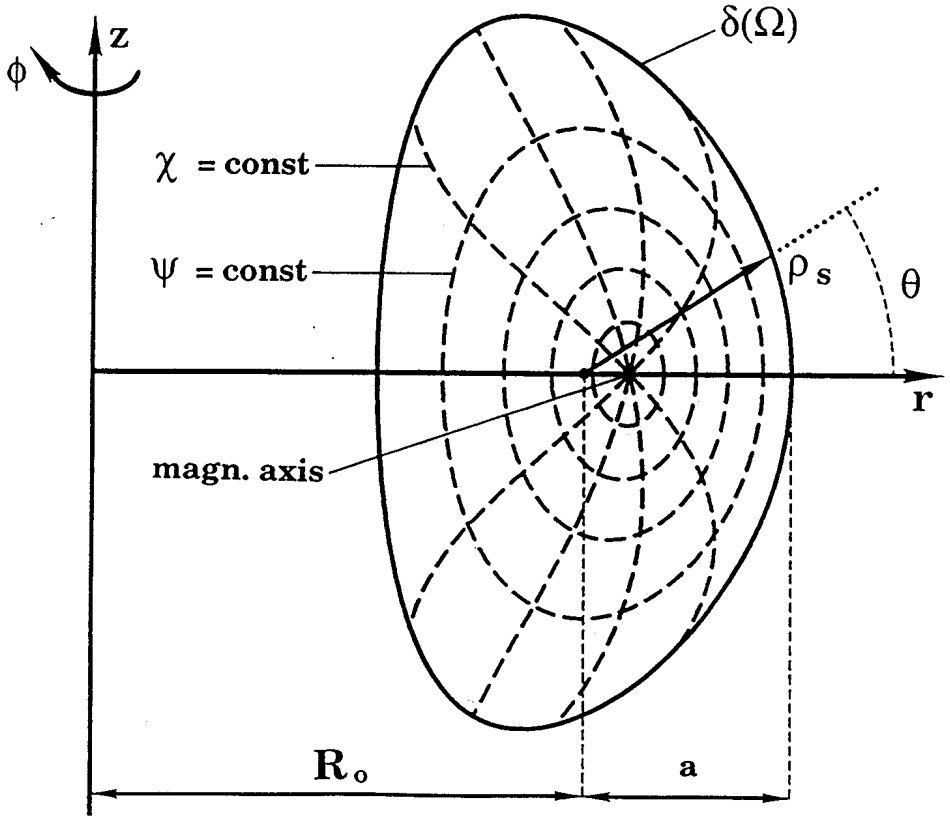

Figure 1: The cylindrical coordinates $(r; z; \phi)$ in toroidal geometry.

2.2 Method of Solution

2.2.1 Variational Problem with Hermite Bicubic Elements

For the spatial discretization, the plasma cross section Ω with ϕ-constant is subdivided into $N_x \times N_y$ rectangular cells, where $(x;y)$ are general coordinates such that $x_0 < x_1 < \ldots < x_i < x_{i+1} < \ldots < x_{Nx}$, $i = 0,\ldots,N_x - 1$ and $y_0 < y_1 < \ldots < y_j < y_{j+1} < \ldots < y_{Ny}$, $j = 0,\ldots,N_y - 1$; both meshes can be spaced arbitrarly. Equation (4) is then solved by the Ritz-Gallerkin method projected on standard Hermite bicubic subspaces [7].

It has been shown [1] that the stepness of the convergence curve of equation (4) strongly depends on the representation of the boundary $\delta(\Omega)$ in the coordinates x and y used for the discretization. For most geometries of interest, $\delta(\Omega)$ is badly approximated by cartesian or polar coordinates. The use of a modified polar coordinate system $(x;y) = (\sigma;\theta)$, where

$$\begin{aligned} r &= \sigma\rho_s(\theta)\cos\theta + r_0 \\ z &= \sigma\rho_s(\theta)\sin\theta + z_0 \end{aligned} \tag{5}$$

has the great advantage that $\delta(\Omega)$ is exactly described by $\sigma = 1$.

2.2.2 Boundary Conditions on Quasipolar Mesh $(\sigma;\theta)$

The boundary condition $\Psi \equiv 0$ on $\delta(\Omega)$ is fulfilled by the bicubic expansion of Ψ if for every $\theta_j, j = 1,\ldots,N_\theta$

$$\begin{aligned} \Psi(\sigma = 1;\theta_j) &= 0 \\ \Psi_\theta(\sigma = 1;\theta_j) &= 0 \end{aligned} \tag{6}$$

The axis of the $(\sigma;\theta)$ mesh is more difficult to treat, because we have to impose Ψ = const and $|\nabla\Psi|$ = const on all the N_θ nodes where $\sigma = 0$, in order to satisfy the regularity of cubic Hermite elements. The behaviour of the solution of problem (4) around the axis is determined up to second order by the expansion in power series

$$\Psi = \Psi_c + \sigma\rho_s(\theta)[\Psi_r cos(\theta) - \Psi_z sin(\theta)] + \mathcal{O}([\sigma\rho_s(\theta)]^2) \tag{7}$$

where Ψ_c, Ψ_r and Ψ_z are unknown. The limit $\sigma \to 0$ of equation (7) gives

$$\begin{aligned} \Psi(\sigma = 0;\theta) &\equiv \Psi_c \\ \Psi_\theta(\sigma = 0;\theta) &\equiv 0 \\ \Psi_\sigma(\sigma = 0;\theta) &= \Psi_r\rho_s(\theta)\cos\theta - \Psi_z\rho_s(\theta)\sin\theta \\ \Psi_{\sigma\theta}(\sigma = 0;\theta) &= \Psi_r[\dot\rho_s(\theta)\cos\theta - \rho_s(\theta)\sin\theta] \\ &\quad - \Psi_z[\dot\rho_s(\theta)\sin\theta + \rho_s(\theta)\cos\theta] \end{aligned} \tag{8}$$

This is imposed by collocation, i.e. for $\theta_j, j = 1,\ldots,N_\theta$, and the $(4 \cdot N_\theta)$ unknowns Ψ, Ψ_θ, Ψ_σ and $\Psi_{\sigma\theta}$ for $\sigma = 0$ are replaced by three: Ψ_c, Ψ_r and Ψ_z.

2.2.3 Picard Iteration

The nonlinear problem (4) is solved iteratively by a Picard method. Ψ is only defined up to an arbitrary constant, and we limit the problem to the fixed boundary case with $\Psi < 0$ on Ω and $\Psi = 0$ on $\delta(\Omega)$. As a normalization condition for the iteration, one possiblity is to fix the total toroidal current

$$I = \int_\Omega j_\phi \, dS, \tag{9}$$

but there are other possible normalizations, as will be discussed in section 4.3. The pressure profile and toroidal magnetic flux required to define j_ϕ in equation (4) are arbitrary functions of Ψ. To prescribe p and T^2, we impose that

$$\begin{aligned} p(\Psi) &= \lambda \, p^*(\Psi/\Psi_{min}) \\ T^2(\Psi) &= \lambda \, T^{*2}(\Psi/\Psi_{min}) \end{aligned} \tag{10}$$

where p^* and T^{*2} are given functions on the interval $[0;1]$.

The Picard iteration starts with an initial guess Ψ_0 which in our case, is a simple paraboloid. Calling $(\Psi_k; \lambda_k)$ the solution after k Picard iterations, one obtains the solution Ψ_{k+1} by solving

$$\int_\Omega \frac{1}{r} \nabla\Psi_{k+1} \cdot \nabla\eta \, dS + \lambda_k \int_\Omega j^*_{\phi,k} \eta \, dS = 0 \tag{11}$$

Here, η represents an arbitrary function on the same functional space as Ψ. Introducing Ψ_{k+1} into equation (10) permits to compute the new source term $j^*_{\phi,k+1}$, and consequently, to correct λ by demanding

$$I = \lambda_{k+1} \int_\Omega j^*_{\phi,k+1} \, dS \tag{12}$$

The Picard iteration is stopped when λ and Ψ are not altered by more than ϵ between two successive iteration steps, i.e.

$$\begin{aligned} \frac{\|\Psi_{k+1} - \Psi_k\|}{\|\Psi_k\|} &< \epsilon \\ \frac{|\lambda_{k+1} - \lambda_k|}{|\lambda_k|} &< \epsilon \end{aligned} \tag{13}$$

To integrate equations (11) and (12), we use a 16 point gaussian quadrature, which is exact for a polynom of order $\sigma^7\theta^7$.

2.2.4 Solver

This finite element approach leads to a system of linear equations of the form

$$\boldsymbol{A} \cdot \boldsymbol{x}_{k+1} = \boldsymbol{b}_k \tag{14}$$

where $\boldsymbol{x}_{k+1}$ includes all unknowns at Picard step $k+1$, $\boldsymbol{b}_k$ represents the source term at step k. $\boldsymbol{A}$ does not depend of Ψ, and consequently remains unchanged during the Picard

iterations. It is a positive definite symmetric banded matrix which is decomposed by a Gauss elimination method into

$$\boldsymbol{A} = \boldsymbol{L}\boldsymbol{D}\boldsymbol{L}^t \tag{15}$$

where $\boldsymbol{D}$ is diagonal and $\boldsymbol{L}$ is lower triangular. Every Picard iteration requires a backsubstitution, which is numerically not very expensive.

The mapping of the solution of equation (4) to flux coordinates $(\Psi;\chi)$ is difficult unless the magnetic axis $|\nabla\Psi| = 0$ is close to the axis of the $(\sigma;\theta)$ mesh. To obtain this, we have introduced the possibility of changing the mesh size. In a typical run, we start with the polar mesh centred at $(r_0;z_0) = (R_0;0)$, where R_0 is the major plasma radius, and $N_\sigma = N_\theta = 16$. The purpose of this is to locate the position of the magnetic axis sufficiently accurately. The center of the $(\sigma;\theta)$ mesh is then moved onto the magnetic axis. To restart the Picard iteration, we interpolate the old solution onto the new mesh. The number of mesh changes is a free parameter, but to avoid performing more than one $\boldsymbol{L}\boldsymbol{D}\boldsymbol{L}^t$ decomposition when $\boldsymbol{A}$ has a big size, we usually set it to two.

3 Results

3.1 Solovev Equilibrium

Solovev has found a class of analytic equilibria [8] for which (4) reduces to a linear equation for Ψ. These equilibria are characterised by

$$\begin{aligned} P(\Psi) &= -\frac{1+E^2}{ER_0^3q_0}\Psi \\ T(\Psi) &= T_0 = 1 \end{aligned} \tag{16}$$

where E denotes the elongation, R_0 and a respectively the major and the minor plasma radius and q_0 the safety factor on the magnetic axis. Replacing equation (16) into equation (4) leads to

$$\Psi = \frac{E}{2R_0^3q_0}\left(\frac{r^2z^2}{E^2} + \frac{\left[r^2-R_0^2\right]^2}{4}\right) - \frac{Ea^2}{2R_0q_0} \tag{17}$$

Here, we have chosen the Solovev equilibrium with $q_0 = 3/4$, $E = 1$, $a = 1/3$ and $R_0 = 1$ as a test case. Figure 2 shows the convergence curve of the poloidal magnetic energy

$$\mathcal{W}_B = \frac{1}{2}\int_{\sigma=0}^{1}\int_{\theta=0}^{2\pi}\sigma\rho_s^2(\theta)\frac{|\nabla\Psi|^2}{r}d\sigma d\theta \tag{18}$$

of the numeric Solovev solution, for an equidistant θ mesh and for a packed θ mesh such that the flux area

$$A_j = \frac{1}{2}\int_{\theta=\theta_j}^{\theta_{j+1}}\rho_s^2(\theta)d\theta \tag{19}$$

is constant for $j = 1,\ldots,N_\theta$. In both cases, the convergence law is $\mathcal{O}(h^6)$, as expected by theory ($h = 1/N_\sigma = 1/N_\theta$ is the width of a cell). The converged value of the poloidal

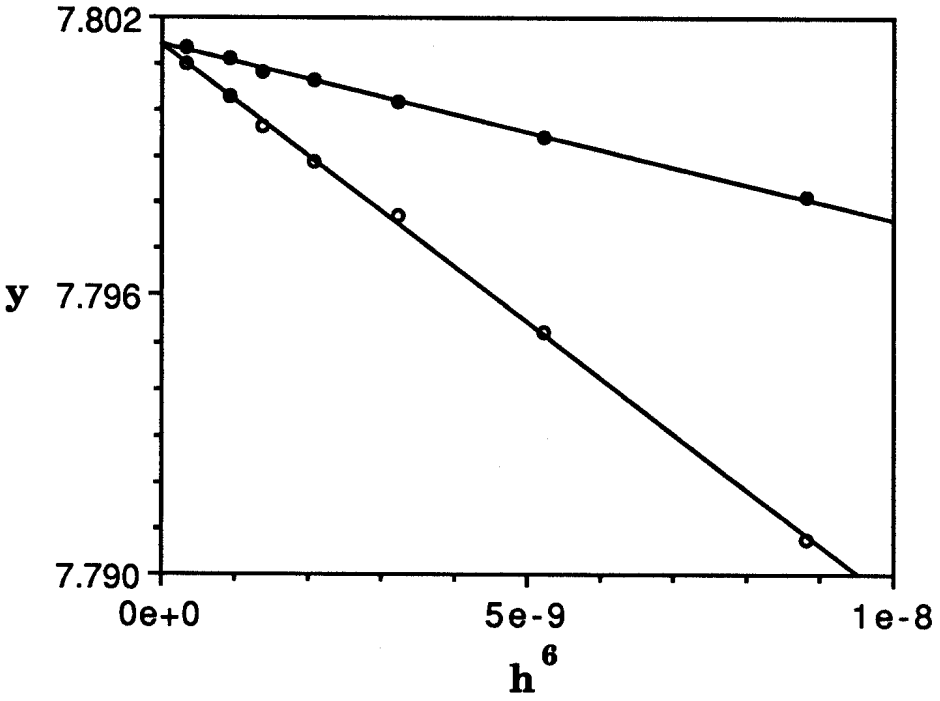

Figure 2: Convergence study of poloidal magnetic energy of the numeric Solovev solution. The poloidal magnetic energy is given by $\mathcal{W}_B = 0.017788 + y \cdot 10^{-7}$. The open (filled) circles are obtained with an equidistant (packed) θ mesh.

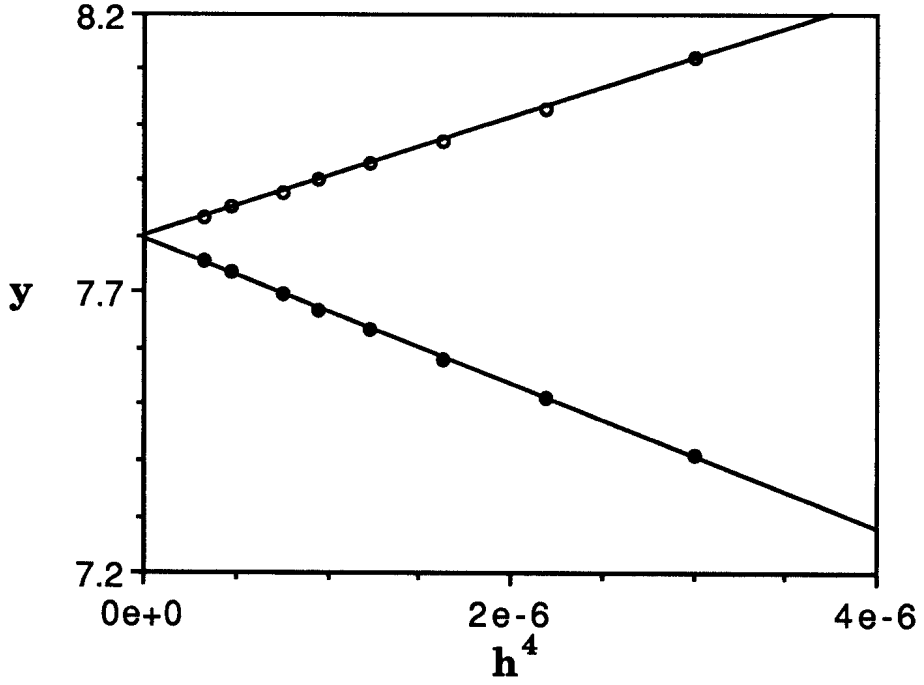

Figure 3: Convergence study of poloidal magnetic energy of the analytic Solovev solution. The poloidal magnetic energy is given by $\mathcal{W}_B = 0.017788 + y \cdot 10^{-7}$. The open (filled) circles are obtained with an equidistant (packed) θ mesh.

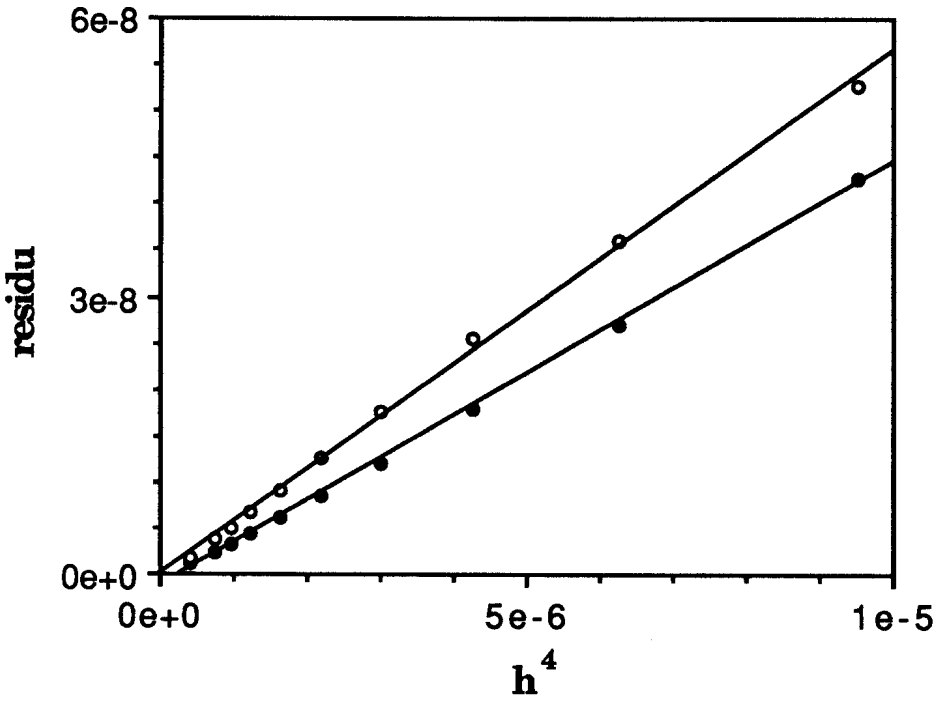

Figure 4: Convergence study of the residu of the Solovev solution on the $(\sigma;\theta)$ mesh nodes. The open (filled) circles are obtained with an equidistant (packed) θ mesh.

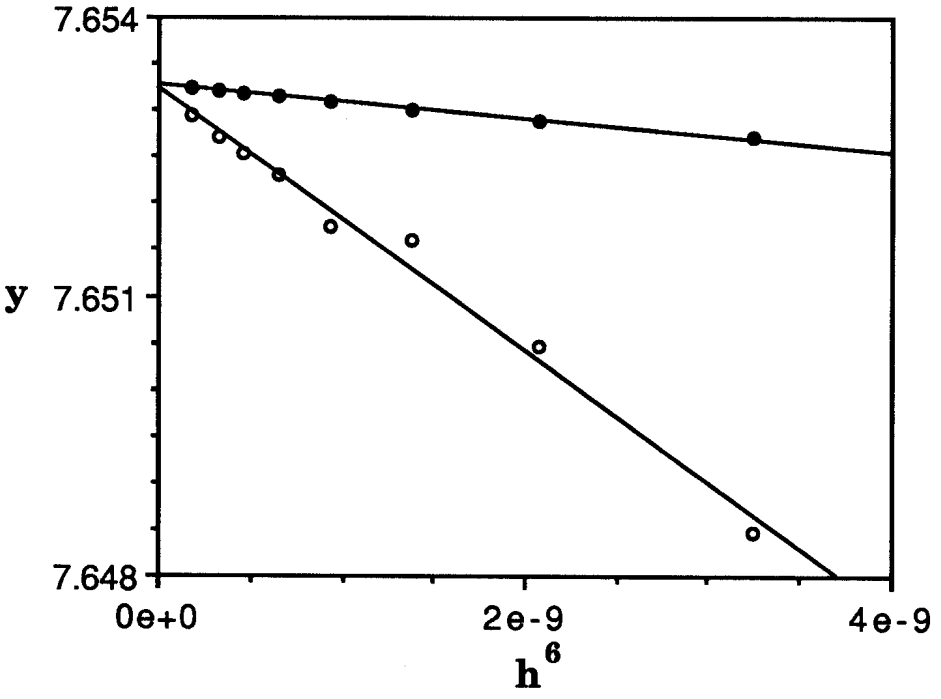

Figure 5: Convergence study of poloidal magnetic energy of the JET test case. The poloidal magnetic energy is given by $\mathcal{W}_B = 0.0201 + y \cdot 10^{-5}$. The open (filled) circles are obtained with an equidistant (packed) θ mesh.

magnetic field is checked by substituting analytical values for Ψ, Ψ_σ, Ψ_θ and $\Psi_{\sigma\theta}$ on the nodes. In this case, the magnetic energy converges as $\mathcal{O}(h^4)$, (see figure 3) because the solution is given by bicubic expansions everywhere, except on the$(\sigma;\theta)$ mesh nodes. The Ritz-Gallerkin method minimizes the error in the poloidal magnetic energy. This can be observed by comparing figure 2 and 3.

In figure 4, we present the convergence of the magnetic flux towards the analytic solution on the $(\sigma;\theta)$ mesh nodes. The convergence rate is $\mathcal{O}(h^4)$, as predicted for local quantities by equation (1). The slopes of the curves in figure 2 and 4 are smaller for the packed θ mesh.

3.2 JET Equilibrium

As a nonlinear test case, we have taken an equilibrium with JET geometry. The plasma surface is defined by

$$\begin{aligned} r &= R_0 + a\cos(\theta + \delta\sin\theta) \\ z &= Ea\sin\theta \end{aligned} \tag{20}$$

where a, E and R_0 have the same meaning as in equation (16), and δ is the triangularity. The parameters for JET are $a/R_0 = 0.423$, $E = 1.68$, $\delta = 0.3$ and $R_0 = 2.96m$. To satisfy the normalization condition (9), we impose the total toroidal current $I = 6.80$ MA with a toroidal magnetic field of 3.5 T, which corresponds to $q_0 = 0.8$. For the two free functions given by equation (10), we have chosen

$$\begin{aligned} P^*(\Psi/\Psi_{min}) &= 0.01(\Psi/\Psi_{min})^2 \\ T^{*2}(\Psi/\Psi_{min}) &= 1.0004055 - 4.0455.10^{-4}(\Psi/\Psi_{min})^2 \end{aligned} \tag{21}$$

The volume averaged beta is 3.96 %. The convergence curves of the poloidal magnetic energy (18) on an equidistant θ and a packed θ mesh defined by equation (19) converge in $\mathcal{O}(h^6)$ (see figure 5). Comparing figure 2 and 5, we see that packing the θ mesh influences the slope of the convergence curve much more for the JET case than for the Solovev case. This is a consequence of the elongation and the triangularity of the JET plasma cross section.

4 Mappings for ERATO and MARS

4.1 Computation of Poloidal Flux Surface Integrals

In this section, we discuss the mapping of the equilibrium into the flux coordinates required by the two stability codes ERATO [4] and MARS [5]. ERATO is an ideal MHD stability code using the so called hybrid finite elements in both the radial and poloidal directions. MARS is a resistive MHD stability code that uses Fourier decomposition in the poloidal angle and finite differences in the radial direction. The metric in the poloidal plane of both stability codes differs completely from the one used for the

equilibrium calculation. The radial stability coordinate of the two codes is

$$s = \sqrt{\frac{\Psi_{min} - \Psi}{\Psi_{min}}} \tag{22}$$

The angular variable χ is defined by the choice of the Jacobian J of the mapping from $(\Psi; \chi; \phi)$ space to cartesian coordinates. In the equilibrium code, J is restricted to the form

$$J = \frac{1}{\nabla\Psi \cdot (\nabla\chi \times \nabla\phi)} = \frac{r}{|\nabla\Psi \times \nabla\chi|} = C(\Psi) r^{\alpha} |\nabla\Psi|^{\mu} \tag{23}$$

where α and μ are integers. $C(\Psi)$ is a function of Ψ only, and is obtained by normalizing χ such that $\chi(2\pi) = 2\pi$. To obtain its explicit expression, we let $\boldsymbol{dl}$ be the arc length element along $\Psi = \text{const}$,

$$d\chi = \nabla\chi \cdot \boldsymbol{dl} = \frac{r dl}{J|\nabla\Psi|} = \frac{r^{(1-\alpha)} dl}{C(\Psi)|\nabla\Psi|^{(\mu+1)}} \tag{24}$$

and the normalization of χ leads to

$$C(\Psi) = \frac{1}{2\pi} \oint_{\Psi=cte} \frac{r^{(1-\alpha)} dl}{|\nabla\Psi|^{(\mu+1)}} \tag{25}$$

By expressing dl in the equilibrium coordinates $(\sigma; \theta)$, we obtain with equation (24) that

$$d\chi = \frac{r\sigma\rho_s^2(\theta)}{J\partial\Psi/\partial\sigma} d\theta \tag{26}$$

This expression permits the integration of quantities along constant Ψ surfaces

$$\mathcal{F}(\Psi = \text{ const }; \chi) = \int_0^{\chi} f(\Psi; \Psi_\sigma; \Psi_\theta; \Psi_{\sigma\theta}; \Psi_{\sigma\sigma}; \Psi_{\theta;\theta}) d\chi' \tag{27}$$

needed by the two stability codes. Certain numerical problems remain due to the use of Hermite elements. We remind that even a simple trapezoidal integration rule applied to equation (27) has an error proportional to the second derivative of the integrand. The Hermite cubic elements do not demand continuity on the cell edges for $\Psi_{\sigma\sigma}$ and $\Psi_{\theta\theta}$. Thus, to perform integrals of the type (27) accurately, the integration interval is split into a set of subintervals delimited by the intersections of the constant Ψ surfaces with the $(\sigma; \theta)$ cell edges. Over each subinterval, the integrand of equation (27) is C^{∞} and a high order integration scheme can be applied (a 4 point gaussian quadrature in our case).

The non-orthogonality

$$\beta_{\Psi\chi} = \frac{\nabla\Psi \cdot \nabla\chi}{|\nabla\Psi|^2} \tag{28}$$

is obtained by

$$d\beta_{\Psi\chi} = \left(\frac{r j_\phi}{|\nabla\Psi|^2} + (2-\alpha) \left[\frac{\partial(\ln r)}{\partial\Psi} \right]_n - (\mu+2) \left[\frac{\partial(\ln|\nabla\Psi|)}{\partial\Psi} \right]_n - \frac{C'(\Psi)}{C(\Psi)} \right) d\chi \tag{29}$$

The index n in equation (29) stands for the normal derivative with respect to Ψ, j_ϕ is defined by equation (4) and $C'(\Psi)$ is derived from the periodicity condition $\beta_{\Psi\chi}(0) = \beta_{\Psi\chi}(2\pi)$.

If we set $\alpha = 2$ and $\mu = 0$, $(\Psi;\chi;\phi)$ becomes the PEST-1 coordinate system with straight field lines and the normalization condition (25) defines the safety factor

$$q(\Psi) \equiv C(\Psi)T(\Psi) = \frac{T(\Psi)}{2\pi} \oint_{\Psi=cte} \frac{dl}{r|\nabla\Psi|} \tag{30}$$

All equilibrium quantities calculated by CHEASE for the stability codes are presented in Appendix A for ERATO and in Appendix B for MARS. It is clear that an integral such as (27) is computed easily on the $(\sigma;\theta)$ mesh only if the mesh axis is situated inside the first flux surface. This is the reason for the mesh shift mentioned in section 2.2.4.

4.2 Convergence Studies of the Mappings

The Solovev equilibrium described in section 3.1 permits to avoid the resolution of the problem (14), because we can substitute analytic values for Ψ, Ψ_σ, Ψ_θ and $\Psi_{\sigma\theta}$. Consequently, the mappings can be completely decoupled from the equilibrium solver in this case, and the convergence properties of the equilibrium quantities as well as the accuracy of the integration scheme presented in section 4.1 can be checked independently.

The convergence properties of the mappings are checked by observing the growth rate of the most unstable linear eigenmode, keeping the stability meshes fixed (for ERATO, $(N_s;N_\chi) = (100;100)$, and for MARS, $(N_s;N_m) = (110;11)$, where N_m is the number of modes used for the poloidal Fourier decomposition). For the Solovev test case, we have computed the growth rate for toroidal mode number $n = 3$, with a perfectly conducting wall at the plasma edge. With the analytic solution vector, both mappings show a convergence rate in $\mathcal{O}(h^4)$, while for the numeric solution, no evident scaling can be extracted, because the scattering of the curve is comparable with its global variation (see figure 6 for ERATO and figure 7 for MARS). The error on the growth rate is smaller with the numeric solution because the finite element representation minimizes errors in a global sense. The values of the growth rates after convergence of the equilibrium are different in figure 6 and 7 because of different truncation errors in the two stability codes.

The JET case described in section 3.2 shows a $n = 1$ instability even with a perfectly conducting wall on the plasma edge. The stability calculation for this equilibrium is more delicate than for the previous test case, because of the presence of several rational safety factor surfaces in the plasma ($q_0 = 0.8$ on the magnetic axis and $q_{edge} \approx 5.4$ at the plasma edge). MARS shows a convergence rate in $\mathcal{O}(h^6)$ in figure 9, whereas with ERATO, the convergence curve is diffuse (see figure 8). The reason for this is probably that ERATO uses finite elements in the poloidal plane, which implies that every small fluctuation of the equilibrium solution is interpreted as a high m mode. This problem does not arise with MARS, because the high m modes are truncated.

For the two test cases, the χ coordinate defined by the constant volume Jacobian ($J = C(\Psi)$ or $\alpha = 0$ and $\mu = 0$ in equation (23)) gives good results for the stability

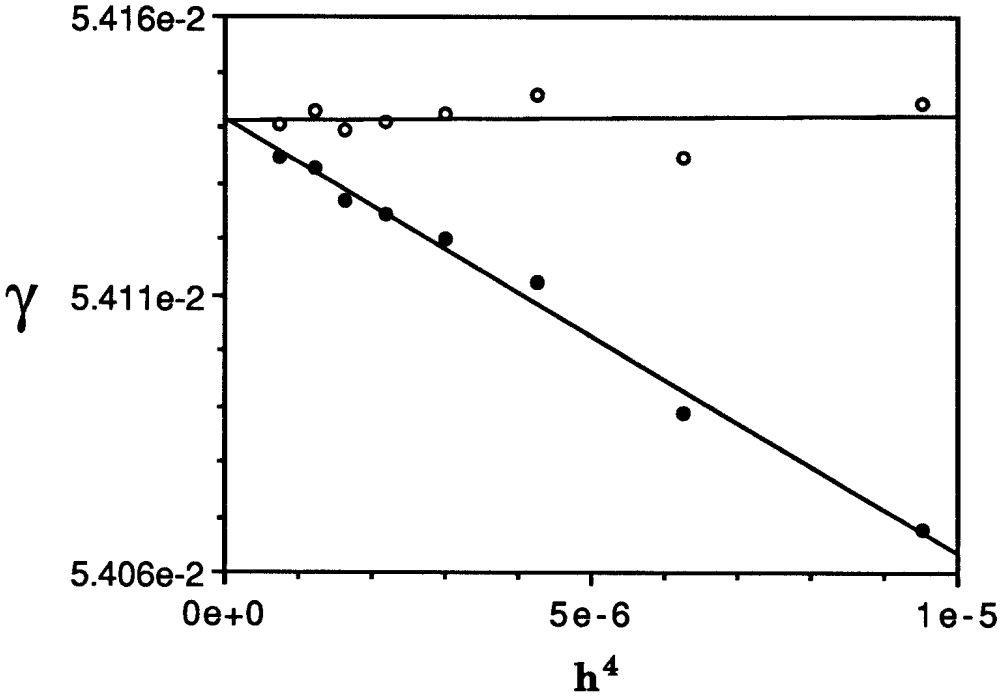

Figure 6: Convergence study of the Solovev test case with ERATO. The filled (open) circles are obtained with the analytic (numeric) equilibrium solution vector.

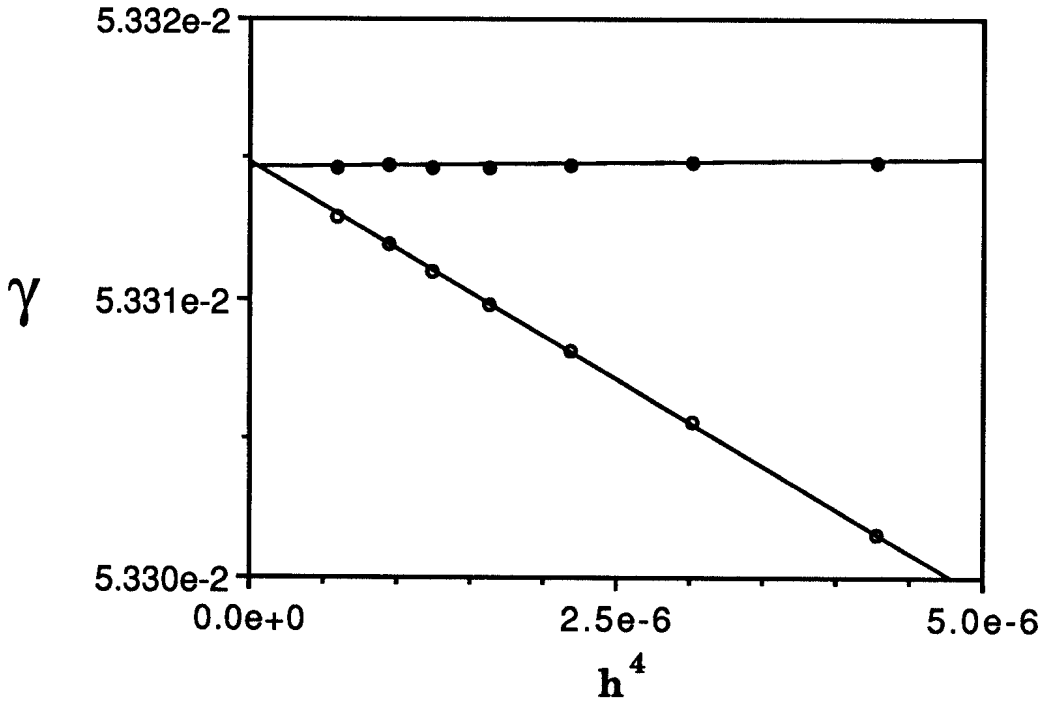

Figure 7: Convergence study of the Solovev test case with MARS. The filled (open) circles are obtained with the analytic (numeric) equilibrium solution vector.

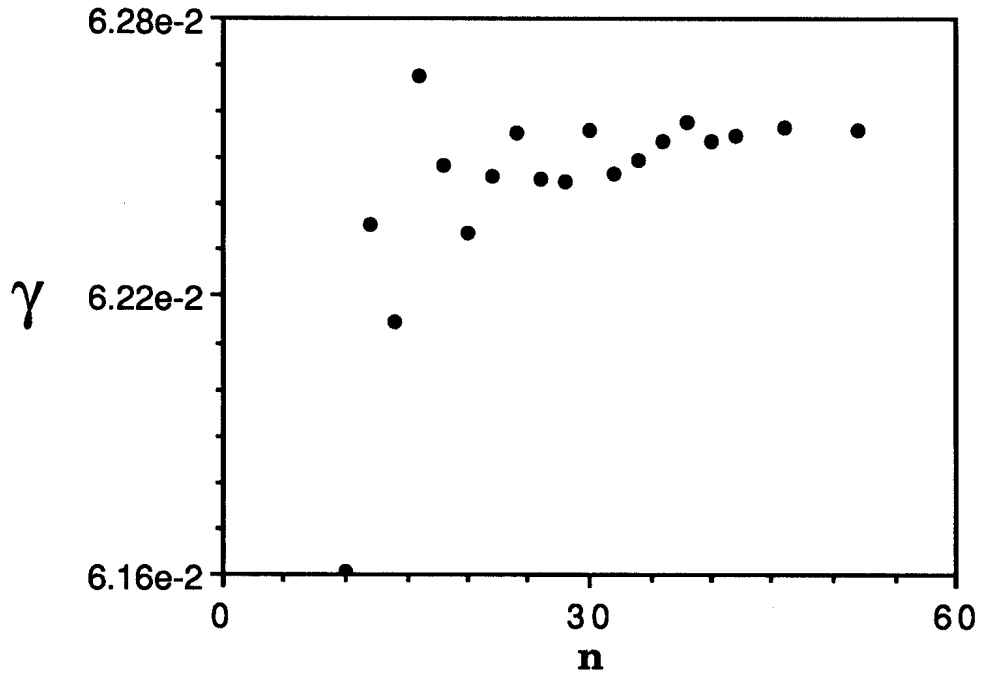

Figure 8: Convergence study of the JET test case with ERATO.

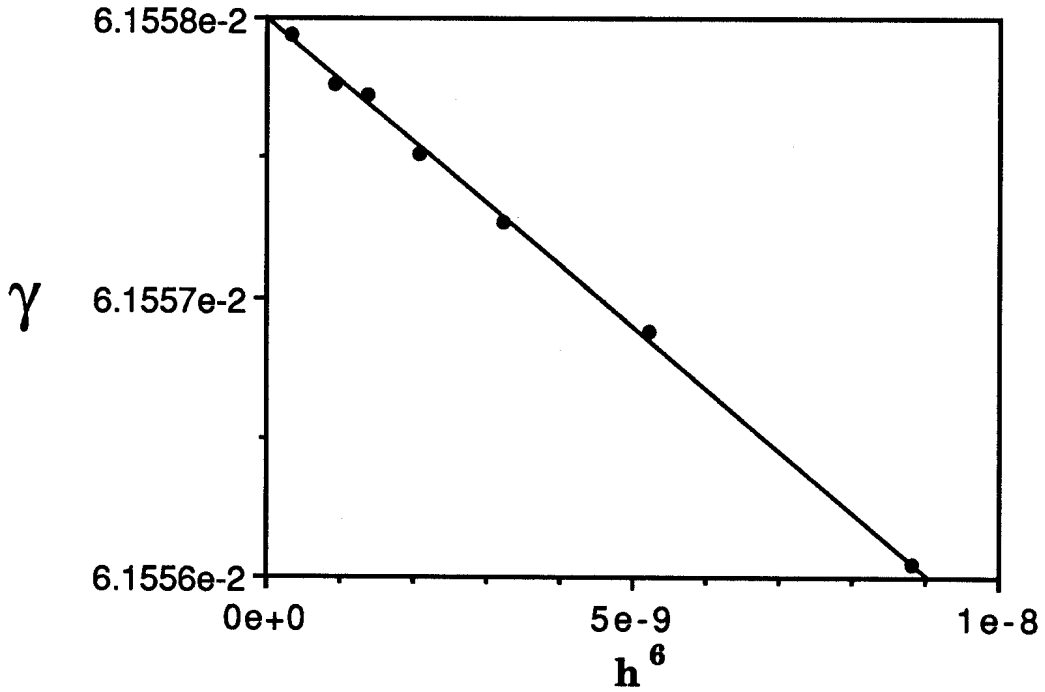

Figure 9: Convergence study of the JET test case with MARS.

calculations (far better than with straight field lines). It must be emphasized that the error on the growth rate due to the equilibrium is negligible in comparison with the error due to the stability calculation itself. The converged value of the growth rate with fixed equilibrium mesh ($N_\sigma = N_\theta = 30$) is $\gamma = 5.395 \cdot 10^{-2}$ for the Solovev test case and $\gamma = 6.198 \cdot 10^{-2}$ for the JET test case with both stability codes. Thus, the error on γ resulting from the equilibrium calculation with a 12×12 mesh is already less than the one due to the stability calculation for MARS with $(N_s; N_m) = (110; 11)$ or for ERATO with $(N_s; N_\chi) = (100; 100)$. For the stability calculations with ERATO, the s mesh is packed on the rational safety factor surfaces ($q = 1$ for the Solovev test case and $q = 1, 2, 3, 4, 5$ for the JET test case). For MARS it has been kept equidistant.

4.3 Scaling transformations of the Equilibrium

With one solution of the variational problem (4), a whole set of equilibria can be generated by changing the normalization condition (9) and by using the fact that T^{*2} is only defined up to an arbitrary constant. There are two basic scaling operations. The first is a multiplication of the poloidal field Ψ by an arbitrary constant. The second is a shift of T^2. These two operations can be combined to specify T at a given surface ($T = 1$ either in the vacuum or on the magnetic axis) and either q on an arbitrary flux surface, or the total toroidal current I defined by (9).

After the scaling of the solution, all relevant physical quantities characterising the equilibrium can be computed. A list of these quantities is given in Appendix C.

5 Extensions of the Code

5.1 Specification of the I'^*_N and the p'^* profiles

It has been found useful in beta-optimization studies [2] to modify the definition of the current profile from that obtained by specifying p'^* and the TT'^{*2}. Instead, we can prescribe the surface averaged toroidal current density

$$I'^*_N(\Psi/\Psi_{min}) = \left(\oint_{\Psi=cte} j^*_\phi (J/r) d\chi\right) / \left(\oint_{\Psi=cte} (J/r) d\chi\right) \tag{31}$$

and the p'^* profile. According to (4), I'^*_N can be written in terms of the three integrals

$$\begin{aligned} C_0 &= \oint_{\Psi=cte} (J/r) d\chi \\ C_1 &= \oint_{\Psi=cte} J d\chi \\ C_2 &= \oint_{\Psi=cte} (J/r^2) d\chi \end{aligned} \tag{32}$$

This gives us an expression for TT'^* on a constant flux surface :

$$TT'^* = -\frac{C_0}{C_2} I'^*_N - \frac{C_1}{C_2} p'^* \tag{33}$$

This profile specification introduces a new iteration over the problem (4) and the mapping, which stops if the residue on the values of the integrals (32) is less than ϵ between two successive iteration steps.

5.2 Ballooning Stability, Mercier and Resistive Interchange Criterion

Ballooning modes are toroidal modes with infinite toroidal mode number n [9,10]. The potential energy for these modes is given by

$$\delta\mathcal{W}_p(n\to\infty)=\frac{1}{2}\int_{-\infty}^{+\infty}\left\{f\left|\frac{\partial\xi}{\partial\chi}\right|^2+g|\xi|^2\right\}Jd\chi \tag{34}$$

where ξ is the radial component of the displacement vector, and χ is a generalized poloidal angle extending from $-\infty$ to $+\infty$. For ballooning stability, $\delta\mathcal{W}_p$ must be positive definite on each flux surface. The quantities appearing in (34) are [9]

$$\begin{aligned}
\nu &= \frac{JT}{r^2}\\
f &= \frac{1}{J^2|\nabla\Psi|^2}\left(1+\frac{r^2|\nabla\Psi|^4}{T^2+|\nabla\Psi|^2}\bar{G}^2\right)\\
g &= -\frac{2r^2p'}{T^2+|\nabla\Psi|^2}\left[\left(\frac{\partial\tilde{P}}{\partial\Psi}\right)_n-\frac{r^2T\bar{G}}{(T^2+|\nabla\Psi|^2)}\frac{1}{J}\left(\frac{\partial\tilde{P}}{\partial\chi}\right)_\Psi\right]\\
\bar{G} &= \nu\beta_{\Psi\chi}+\int_{\chi_0}^{\chi}\left(\frac{\partial\nu}{\partial\Psi}\right)_\chi d\chi'=\frac{\partial}{\partial\Psi}\left(\int_{\chi_0}^{\chi}\nu d\chi'\right)_n\\
\tilde{P} &= p+\frac{1}{2r^2}(T^2+|\nabla\Psi|^2)
\end{aligned} \tag{35}$$

The integral (34) is solved on the $(\Psi;\chi)$ mesh of ERATO by a hybrid linear finite element method. The diagonalization of the matrix corresponding to the variation of problem (34) is not unique. But according to Sylvester's theorem [11], the number of positive terms in the diagonal matrix is invariant. Therefore, if all eighenvalues are positive, the surface is balooning stable.

The Mercier stability [12] and the resistive interchange criterion [13] are checked on every constant poloidal flux surface. Let us define the integrals

$$\begin{aligned}
J_1 &= \frac{1}{2\pi}\oint_{\Psi=cte}\frac{1}{r^2|\nabla\Psi|^2}Jd\chi \quad ; \quad J_2 = \frac{1}{2\pi}\oint_{\Psi=cte}\frac{1}{|\nabla\Psi|^2}Jd\chi\\
J_3 &= \frac{1}{2\pi}\oint_{\Psi=cte}\frac{r^2}{|\nabla\Psi|^2}Jd\chi \quad ; \quad J_4 = \frac{1}{2\pi}\oint_{\Psi=cte}\frac{1}{r^2}Jd\chi\\
J_5 &= \frac{1}{2\pi}\oint_{\Psi=cte}Jd\chi \quad ; \quad J_6 = \frac{1}{2\pi}\oint_{\Psi=cte}\frac{|\nabla\Psi|^2}{r^2}Jd\chi
\end{aligned} \tag{36}$$

A given flux surface is stable to ideal interchanges if the Mercier criterion $-D_I>0$ is satisfied, where

$$-D_I=\left(\frac{p'TJ_2}{q'}-\frac{1}{2}\right)^2+\frac{p'}{q'^2}(J_5'-p'J_3)(T^2J_1+J_4) \tag{37}$$

Resistive interchanges are stable if $-D_R > 0$ with

$$-D_R = -D_I - (H - 1/2)^2 \tag{38}$$

and

$$H = \frac{Tp'}{q'}\left(J_2 - \frac{J_5(J_4 + T^2 J_1)}{J_6 + T^2 J_4}\right) \tag{39}$$

The ' in equation (37) and (39) denotes the derivative with respect to Ψ.

6 Performance on CRAY-2

The cpu-time required on CRAY-2 to compute the two test equilibria presented in section 3 is plotted in figure 10. $n = N_\sigma = N_\theta$ is the size of the equilibrium mesh. The most time consuming operations of the equilibrium solver, the matrix construction and the Gauss elimination, are well vectorized. The tracing of constant poloidal flux surfaces involves many conditional statements, and therefore is not easy to vectorize. This operation is easy to parallelize: each constant poloidal flux surface can be traced by a different processor of the computer. However, this option has not yet been implemented. The cpu-time for the ERATO mapping varies from 13 seconds for $n = 20$ up to 14 seconds for $n = 40$. For MARS, equilibrium quantities are needed on twice as many constant Ψ surfaces as for ERATO. With the same radial mesh size, the cpu-time required by this mapping ranges between 11 seconds for $n = 20$ and 17 seconds for $n = 40$.

The equilibrium solver needs approximatively $4N_\theta N_\sigma(4N_\theta + 300)$ Mwords of central memory storage space, the mapping for MARS $120N_sN_\theta + 50N_sN_m$ Mwords, where N_m is the number of poloidal modes for the Fourier decompostion, and the mapping for ERATO $120N_sN_\theta + 40N_\chi N_s$ Mwords. Consequently, the code may be used only on computers with very large central memory.

7 Conclusion

The Hermite bicubic elements have proved their efficiency for the resolution of the Grad-Schlüter-Shafranov equation. The convergence rates of the equilibrium solution agree with the theoretical predictions, despite the special treatement on the axis of the modified polar mesh used for the discretization. The results presented in section 3 indicate that the value of the constant appearing in equation (1) is very small. This has been confirmed by extensive use of the code.

Furthermore, the method applied to map the equilibrium quantities into flux coordinates is very accurate. The tests shown in this paper demonstrate that, with a reasonable choice of mesh size, the error due to the equilibrium solver on the stability results is negligible compared to the error of the stability computation itself.

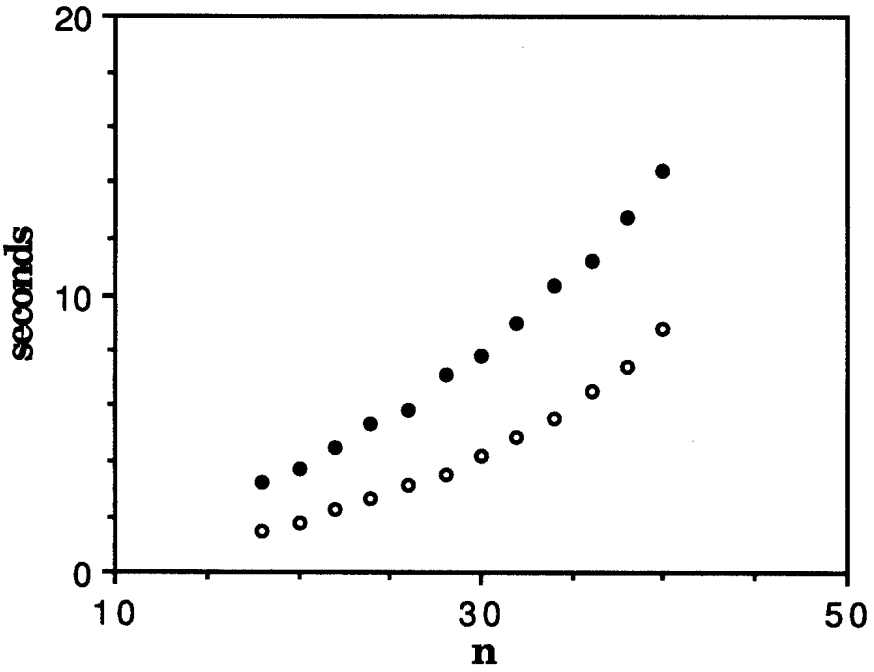

Figure 10: Cpu-time used on CRAY-2 by the equilibrium solver. The filled (open) circles correspond to the computation time of the JET (Solovev) test case.

Acknowledgements

This work was supported in part by the Swiss National Science Foundation.

A Input quantities for ERATO

Let us define the integer mesh $\chi_k = 2\pi(k-1)/N_\chi$ for $k = 1, \ldots, N_\chi + 1$, and the half integer mesh $\chi_{k/2} = (\chi_k + \chi_{k+1})/2$ for $k = 1, \ldots, N_\chi$. Similarly, $s_l = (l-1)/N_s$ for $l = 1, \ldots, N_s + 1$, and $s_{l/2} = (s_l + s_{l+1})/2$ for $l = 1, \ldots, N_s$. For ERATO, all quantities of the equilibrium involved in the stability calculation must be computed at the centers of the stability mesh cells. In Table I, all quantities with $j > 6$ are computed on the $(s_{l/2}; \chi_{k/2})$ mesh, except at the plasma edge. All this informations are stored into an array $EQ(j; k; l)$, for $k = 1, \ldots, N_\chi$ and $l = 1, \ldots, N_s + 1$.

B Input for Linear Resistive Stability Code MARS

MARS uses finite elements in the radial and Fourier decomposition in the poloidal and the toroidal direction. All equilibrium quantities necessary for MARS are directly Fourier transformed in the mapping. For this operation, we apply the integration method described in paragraph 4.1 on

$$f(m; n = 0) = \frac{1}{2\pi} \oint_{\Psi = cte} f e^{im\chi} d\chi \tag{40}$$

where f can be replaced by every EQL in Table II. If a quantity is indexed by i or (and) $i/2$, it is needed on the integer and (or) the half integer s mesh defined in Appendix A. All quantities in table II are expressed as function of the Jacobian

$$J_s = \frac{1}{\nabla s \cdot (\nabla\chi \times \nabla\phi)} = \frac{r}{|\nabla s \times \nabla\chi|} = 2s|\Psi_{min}|J \tag{41}$$

and

$$\beta_{s\chi} = \frac{\nabla s \cdot \nabla\chi}{|\nabla s|^2} = 2s|\Psi_{min}|\beta_{\Psi\chi} \tag{42}$$

where J is given by equation (23) and $\beta_{\Psi\chi}$ by equation(28).

C Global Physical Quantities

All physical quantities computed by the code are listed in Table III. The integral in the χ direction is obtained by the method described in section 4.1, and a trapezoidal rule is applied on integrations in the Ψ direction.

The substitution of equation (3) into the expressions of the local shear and the magnetic field line curvature in Table III gives:

$$\hat{s}_{local} = \frac{T'}{r^2} + \frac{Tj_\phi}{r|\nabla\Psi|^2} - \frac{T}{r^2}\left(\frac{\partial \ln(|\nabla\Psi|^2)}{\partial\Psi}\right)_n \tag{43}$$

and

$$\kappa = \frac{|\nabla\Psi|^2}{(T^2+|\nabla\Psi|^2)}\left[rj_\phi + (T^2+|\nabla\Psi|^2)\left(\frac{\partial \ln(r)}{\partial\Psi}\right)_n + \frac{1}{2}\left(\frac{\partial|\nabla\Psi|^2}{\partial\Psi}\right)_n\right] \tag{44}$$

If we integrate equation (29) and set $\alpha = 2$ and $\mu = 0$, we obtain

$$q'(\Psi) = \frac{1}{2\pi}\int_0^{2\pi} \hat{s}_{local} J d\chi \tag{45}$$

References

[1] R. Gruber, R. Iacono and F. Troyon, *J. Comput. Phys.* **73**, 168 (1987)

[2] A.D. Turnbull, M.A. Secrétan, F. Troyon, S. Semenzato and R. Gruber, *Comput. Phys. Commun.* , 391 (1986).

[3] L.L. Lao, S.P. Hirshman and R.M. Wieland *Phys. Fluids* **24**, 1431 (1981).

[4] R.Gruber, F.Troyon, D. Berger, L.C. Bernard, S. Rousset, R.Schreiber, W. Kerner, W. Schneider and K.V. Roberts, *Comput. Phys. Commun.* **21**, 323 (1981).

[5] A. Bondeson and G. Vlad, *to be published*

[6] J.M. Greene and J.L. Johnson, *Physics Fluids* **5**, 510 (1962).

[7] G. Strang and G. Fix, *An Analysis of the finite element method* (Prentice-Hall, Inc., Englewood Cliffs, N.J., 1973), p.88-89

[8] L.S. Solovev, *Zh. Tekh. Fiz.* **53**, 626 (1967); *JETP* **26**, 400 (1968)

[9] J.W. Connor, R.J. Hastie and J.B. Taylor *Phys. Rev. Lett.* **40**, 396 (1978)

[10] D. Dobrott, D.B. Nelson, J.M. Greene, A.H. Glasser, M.S. Chance and E.A. Frieman *Phys. Rev. Lett.* **39**, 943 (1977)

[11] W. Graeub, *Die Grundlehren der mathematischen Wissenschaften, Band XCVII, Lineare Algebra* (Springer Verlag, Berlin Goettingen Heidelberg, 1958), p.157

[12] C. Mercier *Nucl. Fusion Suppl.* **2**, 801 (1962)

[13] A.H. Glasser, J.M. Greene and J.L. Johnson, *Phys. Fluids* **18**, 875 (1975)

j	$EQ(j;k;l)$
1	s_l
2	χ_k
3	s_{l+1} for $l \neq N_s+1$ and s_{l+1} is free for $l = N_s+1$
4	χ_{k+1}
5	$s_m = (s_l + s_{l+1})/2$ for $l \neq N_s+1$ and $s_m = 1$ for $l = N_s+1$
6	$\chi_m = (\chi_k + \chi_{k+1})/2$
7	mass density ρ
8	plasma pressure $\dfrac{\gamma p}{q_0 \lvert\Psi_{min}\rvert}$
9	toroidal magnetic flux T
10	free
11	q/q_0
12	poloidal magnetic field $\dfrac{\Psi r^2}{q_0 \lvert\nabla\Psi\rvert^2}$
13	non-orthogonality $\beta_{s\chi} = 2s\lvert\Psi_{min}\rvert\beta_{\Psi\chi}$
14	r^2
15	$\left[\dfrac{\partial \ln(r^2)}{\partial s}\right]_\chi$
16	$\left[\dfrac{\partial \ln(r^2)}{\partial \chi}\right]_s$
17	$-2s\lvert\Psi_{min}\rvert\left(\dfrac{r j_\phi}{\lvert\nabla\Psi\rvert^2} - \left[\dfrac{\partial \ln(r^2/J)}{\partial \Psi}\right]_\chi\right)$
18	$\dfrac{2\Psi}{q_0}\left(\dfrac{j_\phi^2}{\lvert\nabla\Psi\rvert^2} - \dfrac{j_\phi}{r}\left[\dfrac{\partial \ln\lvert\nabla\Psi\rvert}{\partial\Psi}\right]_n - p'\left[\dfrac{\partial \ln r}{\partial\Psi}\right]_n\right)$
19	r^2/J
20	$\left[\dfrac{\partial \ln(r^2/J)}{\partial \chi}\right]_\Psi$
21	$\dfrac{\partial}{\partial s}\left[\int_0^\chi \dfrac{JT}{r^2} d\chi'\right]$
22	non-orthogonality $\beta_{s\chi}^{f.c.} = 2s\lvert\Psi_{min}\rvert\beta_{\Psi\chi}^{f.c.}$ with straight field lines
23	$\left[\dfrac{\partial \lvert\nabla\Psi\rvert^2}{\partial \chi}\right]_\Psi$

Table I: Input quantities for ERATO

j	$EQL(j)$	index
1	$\frac{g_{ss}}{J_s} = J_s\left(\beta_{s\chi}\frac{\lvert\nabla s\rvert}{r}\right)^2 + \frac{1}{J_s\lvert\nabla s\rvert^2}$	i, i/2
2	$\frac{g_{\chi\chi}}{J_s} = J_s\left(\frac{\lvert\nabla s\rvert}{r}\right)^2$	i, i/2
3	$\frac{g_{\phi\phi}}{J_s} = \frac{r^2}{J_s}$	i, i/2
4	$\frac{g_{s\chi}}{J_s} = -J_s\beta_{s\chi}\left(\frac{\lvert\nabla s\rvert}{r}\right)^2$	i, i/2
5	$J_s g_{ss}$	i, i/2
6	$J_s g_{\chi\chi}$	i, i/2
7	$J_s g_{\phi\phi}$	i, i/2
8	$J_s g_{s\chi}$	i, i/2
9	J_s	i, i/2
10	$J_s j^{\chi} = -2s\lvert\Psi_{min}\rvert T'(\Psi)$	i
10	$J_s B^{\chi} = 2s\lvert\Psi_{min}\rvert$	i/2
11	$J_s j^{\phi} = -J_s\left[p'(\Psi) + T(\Psi)T'(\Psi)/r^2\right]$	i
11	$J_s B^{\phi} = J_s T(\Psi)/r^2$	i/2
12	$p(\Psi)$	i/2

Table II: Input quantities for MARS

Global quantities			
Total plasma volume / 2π	V_{tot}	$=$	$\int\int J d\Psi d\chi$
Averaged pressure	$\bar{p}$	$=$	$\left(\int\int pJ d\Psi d\chi\right)/V_{tot}$
Averaged p^2	$\bar{p^2}$	$=$	$\left(\int\int p^2 d\Psi d\chi\right)/V_{tot}$
Averaged B^2	$\bar{B^2}$	$=$	$\left(\int\int J[T^2+\lvert\nabla\Psi\rvert^2]/r^2 d\Psi d\chi\right)/V_{tot}$
Total toroidal current	$\bar{I}_\phi$	$=$	$\int\int j_\phi (J/r) d\Psi d\chi$
Plasma inductance	$\mathcal{L}$	$=$	$\frac{2}{\bar{I}_\phi{}^2 R_{mag}}\int\int J\frac{\lvert\nabla\Psi\rvert^2}{r^2}d\Psi d\chi$
Total beta	β	$=$	$\frac{2\bar{p}}{\bar{B^2}}$
Poloidal beta	β_p	$=$	$\frac{8\pi}{\bar{I}_\phi{}^2 R_{mag}}\int\int pJ d\Psi d\chi$
Princeton beta	β^*	$=$	$\frac{2\sqrt{\bar{p^2}V_{tot}}}{\bar{B^2}}$
Flux surface quantities			
Plasma volume within $\Psi=$ const	$V(\Psi)$	$=$	$\int_{\Psi'=\Psi_{min}}^{\Psi}\oint J d\chi d\Psi'$
Toroidal current within $\Psi=$ const	$I_\phi(\Psi)$	$=$	$\int_{\Psi'=\Psi_{min}}^{\Psi}\oint j_\phi (J/r) d\chi d\Psi'$
Poloidal beta on $\Psi=$ const	$\beta_p(\Psi)$	$=$	$\frac{8\pi}{I_\phi^2(\Psi)R_{mag}}\int_{\Psi'=\Psi_{min}}^{\Psi} p(\Psi')\frac{dV(\Psi')}{d\Psi'}d\Psi'$
Global shear on $\Psi=$ const	$\hat{s}(\Psi)$	$=$	$\frac{\rho}{q(\Psi)}\frac{dq}{d\rho}(\Psi)$ where $\rho=\sqrt{V(\Psi)/V_{tot}}$
Local quantities			
Local shear	$\hat{s}_{local}$	$=$	$-\frac{1}{\lvert\nabla\Psi\rvert^4}(\boldsymbol{B}\times\nabla\Psi)\cdot\nabla\times(\boldsymbol{B}\times\nabla\Psi)$
Magnetic field line curvature	κ	$=$	$\frac{1}{B^2}\nabla\Psi\cdot(\boldsymbol{B}\cdot\nabla)\boldsymbol{B}$

Table III: Physical quantities computed by equilibrium code